

## Early-fusion based pulsar identification with smart under-sampling

Shi-Chuan Zhang (张士川)<sup>1,2</sup>, Xiang-Cong Kong (孔祥聪)<sup>1,2</sup>, Yue-Ying Zhou (周月影)<sup>1</sup>,  
Ling-Yao Chen (陈凌曜)<sup>1</sup>, Xiao-Ying Zheng (郑小盈)<sup>1,2</sup>, Chun-Ling Xu (许春玲)<sup>1</sup>,  
Bao-Qiang Lao (劳保强)<sup>3</sup> and Tao An (安涛)<sup>3</sup>

<sup>1</sup> Shanghai Advanced Research Institute, Chinese Academy of Sciences, Shanghai 201210, China; [zhengxy@sari.ac.cn](mailto:zhengxy@sari.ac.cn)

<sup>2</sup> University of Chinese Academy of Sciences, Beijing 100049, China

<sup>3</sup> Shanghai Astronomical Observatory, Chinese Academy of Sciences, Shanghai 200030, China

Received 2020 May 4; accepted 2021 July 2

**Abstract** The discovery of pulsars is of great significance in the field of physics and astronomy. As the astronomical equipment produces a large number of pulsar data, an algorithm for automatically identifying pulsars becomes urgent. We propose a deep learning framework for pulsar recognition. In response to the extreme imbalance between positive and negative examples and the hard negative sample issue presented in the High Time Resolution Universe Medlat Training Data, there are two coping strategies in our framework: the smart under-sampling and the improved loss function. We also apply the early-fusion strategy to integrate features obtained from different attributes before classification to improve the performance. To our best knowledge, this is the first study that integrates these strategies and techniques in pulsar recognition. The experiment results show that our framework outperforms previous works with respect to either the training time or  $F1$  score. We can not only speed up the training time by  $10\times$  compared with the state-of-the-art work, but also get a competitive result in terms of  $F1$  score.

**Key words:** methods: data analysis — (stars:) pulsars: general — techniques: image processing

### 1 INTRODUCTION

A pulsar is a high-speed spinning neutron star which can continuously emit electromagnetic pulse signals. In physical and astronomical studies, the cosmic clocks produced by pulsars can be used as a galactic-scale detector for many fundamental physics applications, including gravitational wave. There are several modern radio telescope survey projects, such as Parkes Multi-beam Pulsar Survey (PMPS) (Keane et al. 2010), High Time Resolution Universe (HTRU) (Keith et al. 2010), Pulsar Arecibo L-band Feed Array survey (PALFA) (Cordes et al. 2006) that are actively scanning the sky and collecting signals for potential pulsar candidates. In a pulsar search procedure, periodic broadband signals exhibiting signs of dispersion from the universe space are collected by the modern radio telescope surveys. These signals are processed and recorded as a pulsar candidate collection of diagnostic plots and summary statistics if they meet some criteria. The pulsar candidate collection is further analyzed manually or automatically to select the prospective candidates for further verification. A pulsar candidate contains a set of diagnostic values and graphical

representations, including the time-versus-phase (TPP), the frequency-versus-phase (FPP), the summed profile plot (SPP), and the dispersion measure (DM) curve, etc. Due to the improving survey specifications, there is an exponential rise in the pulsar candidate numbers and data volumes. The machine learning techniques have recently been introduced to mitigate the scalability issue of the pulsar identification problem (Yao et al. 2016; Zhang et al. 2019; Wang et al. 2017a; Morello et al. 2014; Zhu et al. 2014; An 2019).

There are some open-source pulsar candidate sets such as HTRU Medlat Training Data collected by the HTRU survey (Morello et al. 2014) and Five-hundred-meter Aperture Spherical radio Telescope (FAST) Label Data collected by the Commensal Radio Astronomy FAST Survey (Wang et al. 2019). The HTRU Medlat dataset is a collection of labeled pulsar candidates from the intermediate galactic latitude part of the HTRU survey, which precisely contains 1196 known pulsar candidates from 521 distinct sources, and 89 996 non-pulsar candidates. The FAST dataset contains 837 known pulsar candidates and 998 non-pulsar candidates in the training set; and 326 pulsar candidates and 13 321 non-

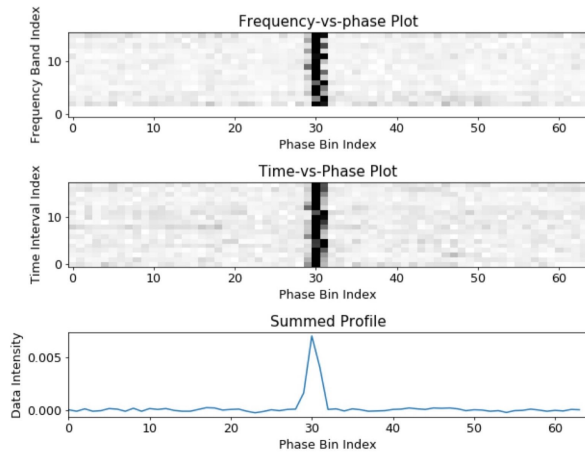


**Fig. 1** A typical positive pulsar candidate in the HTRU Medlat dataset. The periodical signals are processed by the pipeline software to produce a set of diagnostic values and graphical representations including FPP, TPP and SPP. For a real pulsar, there is a bold vertical stripe in both FPP and TPP, and a significant peak in SPP.

pulsar candidates in the testing set, respectively. Hence, the skewness of the dataset is not very severe compared with HTRU. In this paper, we focus on the open-source pulsar candidate set of HTRU Medlat Training Data. We use the code provided by Morello et al. (2014) to generate the attributes of FPP, TPP and SPP for each pulsar candidate, and show two sample candidates in Figure 1 and Figure 2. In Figure 1, in both FPP and TPP, there is a bold vertical stripe; and there is also a significant peak in SPP. Thus this pulsar candidate can be labeled as a positive candidate and will be selected for further verification by astronomers. In Figure 2, there is no bold vertical stripe in neither FPP nor TPP, or no significant peak in SPP. Thus this pulsar candidate can be labeled as negative and will be dropped. As positive and negative candidates present significant differences in FPP, TPP and SPP, a machine learning based pulsar candidate selection approaches can be used to screen the candidates automatically and will be investigated in our paper.

Automatic recognition is an efficient approach to improve pulsar filter efficiency. In general, deep learning is robust with a wide spectrum of applications based on the huge numbers of data, the fast-computing devices and the large capacity storage. However, sometimes it does not work well when the numbers of samples are not balanced between different classes. This phenomenon is called a class imbalance problem. It is claimed that the classification performance of the same deep learning model can be substantially different with the balanced and imbalanced data sets (Padma et al. 2011). With the imbalanced data, the model has preference for the class with more samples than other classes. Therefore,

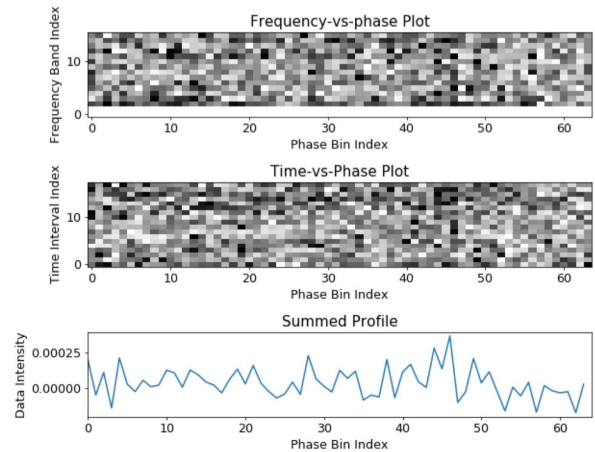


**Fig. 2** A typical negative candidate in the HTRU Medlat dataset. For an RFI signal, there is no bold vertical stripes in neither FPP nor TPP, or no significant peaks in SPP.

the accuracy of test tends to be high, but the recall of the minor class with less samples is low. However, the recall of minor class is usually an important indicator of performance. Unfortunately, the pulsar identification problem suffers from the class imbalance. In a pulsar candidate set, most of the samples are radio frequency interference (RFI) signals that are noise, i.e., negative samples; and only a small set of samples is real pulsars, i.e., positive samples. The ratio of positive sample to negative samples can be up to 1 : 90. Therefore, the negative samples dominate the pulsar candidate dataset and become a huge challenge for pulsar recognition. Furthermore, even for positive pulsars, there exist hard samples. As shown in Figure 1 and Figure 2, there are some real pulsars that present significant difference in diagnostic plots and are easy to identify; and there also exist some hard negative noises that are very similar to real pulsars and are very hard to classify as shown in Figure 3. In Figure 3, the top picture shows the time-versus-phase (TPP) plot of a positive pulsar candidate; and the bottom picture shows the TPP of a negative candidate. Since there is no obvious bold vertical stripe in the TPP of the positive sample, the two TPPs are very similar and hard to differentiate between each other. These candidates are called hard samples.

To overcome the above challenges, we propose a deep-learning based framework for the binary-classification pulsar recognition with imbalanced classes. The framework consists of three stages. At Stage 1, we apply a *smart under-sampling* method which was first proposed by Vannucci & Colla (2016). The smart under-sampling deletes about 86% of the negative samples and retains almost all positive samples by calculating the Mahalanobis distance for each sample. With this smart under-sampling, we can reduce the ratio of positive to negative samples

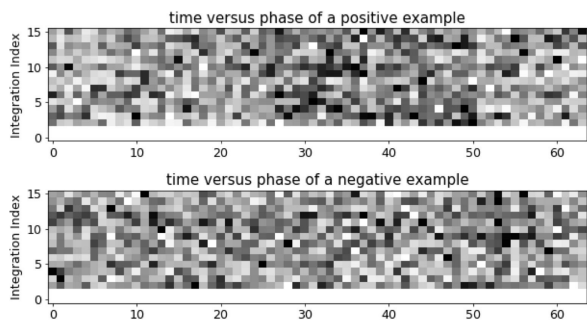


**Fig. 3** Hard samples. The top picture is a TPP of a positive pulsar candidate; and the bottom picture is a TPP of a negative pulsar candidate. There is no obvious bold vertical stripes in the TPP of the positive sample. Both the two TPPs are very similar and are hard to identify.

from 1 : 90 to 1 : 10, which greatly mitigates the class imbalance. At Stage 2, we apply deep learning network models to extract features from the dataset. We select three attributes from the 17 attributes of pulsars, i.e., TPP, FPP and SPP, and extract features for each of the attributes. We apply the  $\alpha$ -balanced loss function to further help the class imbalance issue, and propose to use a  $\gamma$  parameter to down-weight the easy examples and focus on the hard negative examples in the loss function. At Stage 3, we propose the simple attention mechanism to learn the weights of the three features obtained at Stage 2, and blend the features to form a single feature. This is called the *early-fusion* strategy, which was first proposed in Gunes & Piccardi (2005). In the early-fusion, the features are blended before classification; in the meanwhile, the late-fusion strategy proposed in Zhu et al. (2014) and Li et al. (2018) blends the classification results after the classifying operation. Finally, the blended feature is fed into a binary classifier to filter the positive candidates.

We conclude our contribution. We propose a smart under-sampling to solve the class imbalance. We apply the early-fusion based simple attention mechanism to integrate different features obtained from three attributes of pulsars for further classification. We improve the loss function to further help the class imbalance and the hard sample issues. The rest of the paper is organized as follows. In Section 1.1, we investigate the related works. We present our deep learning based pulsar identification framework in Section 2. In Section 3, our framework is evaluated by comparing with the state-of-the-art works. We draw a conclusion in Section 4.

### 1.1 Related Works

There are some successful works for pulsar recognition with machine learning. The earlier approaches focused on the statistical features manually designed by astronomers

(Yao et al. 2016; Wang et al. 2017a). Recently, some data-driven deep learning models have emerged. Zhu et al. proposed a pulsar image-based classification system (PICS) (Zhu et al. 2014). PICS uses the single-hidden-layer artificial neural network (ANN), the support vector machines (SVMs), and the convolutional neural networks (CNNs) to process different features, and assembles the networks together with a logistic regression classifier to construct the PICS. The overall architecture does not consider the imbalanced issue. The plain CNN networks are used to classify the TPP and FPP plots, and a simple weighted strategy is used to assemble different classifiers. Nevertheless, the work proposed by Zhu et al. demonstrates the capability and advantages of the CNNs for pulsar candidate selection task. In Wang et al. (2019), Wang et al. further improved PICS by replacing the CNNs with a residual network model comprising 15 layers. The work in Wang et al. (2019) does not consider the class imbalance either. In Guo et al. (2017), Guo et al. used the deep convolution generative adversarial networks (DCGAN) and the SVM to extract features and classify pulsar candidates. Li et al. used a hierarchical model to identify the pulsars with four diagnostic plots as inputs in Li et al. (2018). They reduced the running time of the complex model with a pseudo-inverse learning algorithm. There are some other data-driven methods for pulsar recognition such as Zhu et al. (2014) and Morello et al. (2014). The advantage of data-driven approaches is that they do not require to manually extract features and finish tasks. The framework proposed in this paper is also a data-driven approach.

A lot of works have been investigated to cope with the unbalanced classification. In the survey of the unbalanced binary classification (Gao et al. 2018), Gao et al. grouped different approaches into two categories: data-level methods and algorithm-level methods. The data-level methods include re-sampling and ensemble learning. The re-sampling approach balances the data set by repeatedly sampling positive samples (Chawla et al. 2002; Han et al. 2005; He et al. 2008), or under-sampling negative samples (Wilson 1972; Tomek 1976). For example, Zhang et al. used the random over-sampling to classify pulsar candidates in Zhang et al. (2019). Re-sampling algorithms with preference for specific samples are proposed in Vannucci & Colla (2016), Vannucci & Colla (2017) and Vannucci & Colla (2018). The ensemble learning approach builds multiple subsets of the majority class by random under-sampling. Each of the under-sampled majority subsets is united with the minority class to create a balanced data set. Based on these balanced under-sampled data set, weak classifiers are trained and integrated through voting or weighting to build the overall classifier. The work in Liu et al. (2009) proposes two ensemble

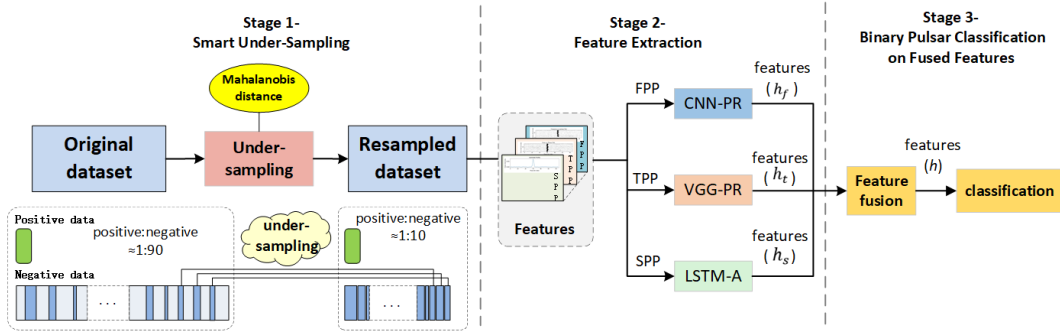


**Fig. 4** The learning framework consists of three stages. At Stage 1, the original HTRU Madlat dataset is cleaned by the smart under-sampling. After cleaning, 85% of data are washed away and the dropped data are almost negative samples. At Stage 2, the data after cleaning are used to train and test fine classifiers to extract features of diagnostic plots. At Stage 3, we train and test a neural network that can fuse features for classification. The fused features are finally fed into a binary pulsar/noise classifier.

learning models as EasyEnsemble and BalanceCascade. EasyEnsemble combines the learners that are trained from multiple subsets of the majority class. BalanceCascade trains the learners sequentially, where the majority class examples that are correctly classified by the current trained learners are removed at each training step. Algorithm-level methods generally apply cost-sensitive functions to tune sample weights. In Zhou et al. (2017) and Lin et al. (2020), the improved loss function is used for the single-target tracking problem and the objects detection, where the quantities of positive samples and negative samples are unbalanced. A hybrid feature selection algorithm is proposed in Zhang et al. (2018) to process the unbalanced data problem when the data has multiple features. The work in Guo et al. (2017) uses the DCGAN architecture to generate pulsar samples to solve the unbalanced issue.

Next, we investigate feature fusion. A proper feature fusion strategy can greatly improve the classification accuracy. In Chaib et al. (2017), a discriminant correlation analysis (DCA) was adopted as the feature fusion strategy to refine the original features, which is more efficient than the traditional feature fusion strategies. The attention mechanism is widely used in visual tasks. A feature fusion method based attention mechanism was proposed for the video classification in Long et al. (2018). In Wang et al. (2017b), the authors designed a residual attention network (RAN) to generate attention-aware features.

## 2 A DEEP LEARNING FRAMEWORK FOR PULSAR IDENTIFICATION

The challenge faced by pulsar candidate selection is the extreme imbalance between positive and negatives samples in the dataset. In this section, we propose a novel learning framework integrating three techniques including smart undersampling, improved cross entropy loss and attention-based feature fusion, to cope with the data imbalance as shown in Figure 4.

### 2.1 Stage 1: Smart Under-Sampling

The HTRU Medlat Training Data set contains 1196 known pulsar samples and 89996 non-pulsar samples, which results in a positive-to-negative-sample ratio of nearly 1 : 90. We propose to remove most of the non-pulsar samples from the dataset with a smart under-sampling technique. The intuition behind the smart under-sampling is that most non-pulsar samples are noise and follow the normal distribution. We focus on removing those noise data points that perfectly fit in the normal distribution and leave the legitimate pulsar candidates and other RFI/noise samples to be classified by the machine learning algorithm. Outlier detection is the identification of data points that differ significantly from other observations. In our case, the outlier detection is used to identify the data points that do not follow the normal distribution. In the ideal case, we hope all legitimate pulsar candidates will be identified as outliers.

$$D_M(\mathbf{x}) = \sqrt{(\mathbf{x} - \mu)^T \Sigma^{-1} (\mathbf{x} - \mu)}. \quad (1)$$

The Mahalanobis distance defined in Equation (1) is a measure of the distance between a point  $\mathbf{x}$  and a distribution (Hubert & Debruyne 2010). In Equation (1),  $\mu$  is the mean vector of the distribution,  $\Sigma$  is the covariance matrix of the distribution, and the notation  $T$  denotes the transpose of a matrix or a vector. The distance is zero if  $\mathbf{x}$  is at the mean  $\mu$ , and grows as  $\mathbf{x}$  moves away from the mean along each principal component axis.

We use the Mahalanobis distance in our outlier detection. Assume the noise points follow a normal distribution, we calculate the Mahalanobis distance  $D_M(\mathbf{x})$  for each candidate  $\mathbf{x}$ . The mean vector  $\mu$  and the covariance matrix  $\Sigma$  are calculated based on the dataset. A sample  $\mathbf{x}$  is considered to be an outlier if  $D_M(\mathbf{x}) \geq c$ , where  $c$  is a threshold. When tuning the threshold  $c$ , it is required to label as many positive pulsar candidates as outliers

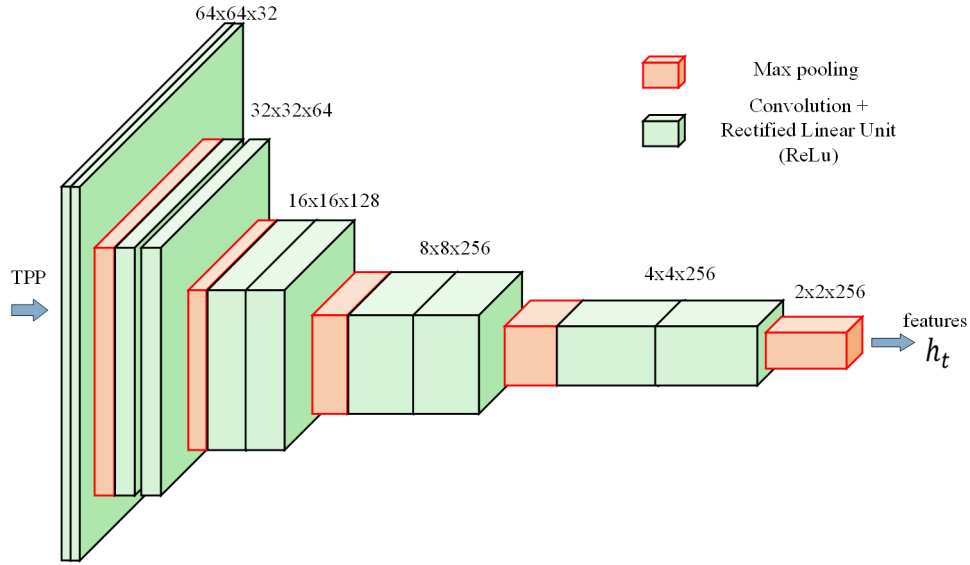


**Fig. 5** The VGG-PR model for processing the TPP plots. It consists of 10 convolutional layers, five pooling layers and a multilayer perceptron (MLP) containing three fully connected layers. The output is the feature vector  $h_t$ . The feature vector  $h_t$  will be fed into Stage 3.

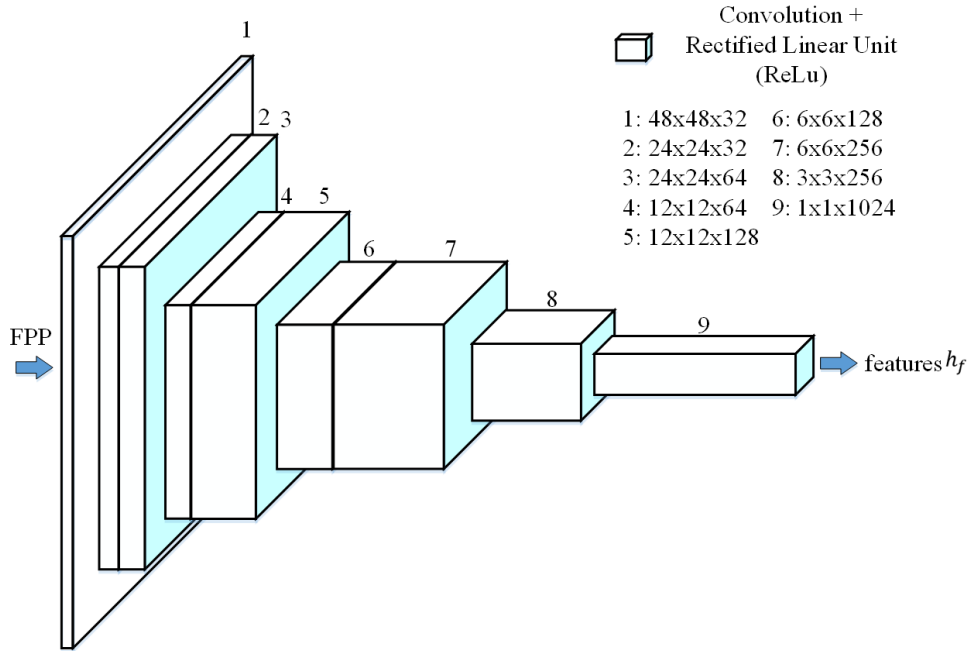


**Fig. 6** The CNN-PR model for processing the FPP plots. It consists of nine convolutional layers and an MLP containing three fully connected layers. The output is the feature vector  $h_f$ . The feature vector  $h_f$  will be fed into Stage 3.

as possible, even if there are many negative candidates labeled as outliers. All the positive and negative samples labeled as outliers will enter Stage 2 in Figure 4 for further process. Thus, the outlier-detection based smart under-sampling efficiently drops the negative samples that closely follow the normal distribution.

We do not apply the smart under-sampling on the original HTRU-Medlat dataset directly, because it is difficult to find an optimal threshold  $c$  with the original

dataset of many attributes. Instead, we apply the smart under-sampling on the dataset of FPP diagnostic plots obtained from the HTRU-Medlat dataset. We also tested the smart under-sampling on the obtained dataset of TPP and SPP. The practical experience found that under-sampling with FPP diagnostic plots keeps all legitimate pulsar candidate and achieves a low positive-to-negative-sample ratio. After the smart under-sampling, the positive-

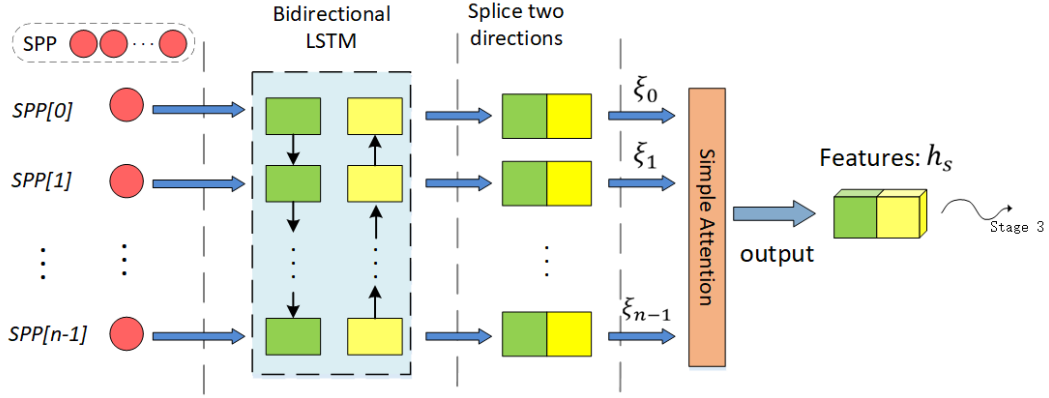


**Fig. 7** The LSTM-A model for processing the SPP sequence. It consists of the bidirectional LSTM, the simple attention mechanism and an MLP containing three fully connected layers. The output is the feature vector  $h_s$ . The feature vector  $h_s$  is fed into Stage 3.

to-negative-sample ratio reduces to nearly 1 : 10, and the imbalanced data problem is alleviated.

## 2.2 Stage 2: Feature Extraction

Three kinds of diagnostic plots, i.e., TPP, FPP and SPP, are used in our learning framework. Since TPP and FPP are presented as images, and SPP is presented as a sequence, they will be processed by different neural network models.

Convolutional neural networks (CNN) are the most commonly applied class of deep neural networks in image processing. Deep convolutional neural network (DCNN) models that are composed of different convolutional layers and pooling layers have achieved excellent performance in image recognition. We apply a DCNN model proposed in Simonyan & Zisserman (2015) (known as VGG13) to process the TPP plots, which is called the VGG for pulsar recognition (VGG-PR). As shown in Figure 5, our VGG-PR model consists of 10 convolutional layers, five pooling layers and three fully connected layers. Compared with the original VGG13 model proposed in Simonyan & Zisserman (2015), our VGG-PR model has a larger convolution kernel and fewer channels. For processing the FPP plots, a DCNN structure containing nine convolutional layers and three fully connected layers is used in our learning framework, which is called the CNN for pulsar recognition (CNN-PR). We choose different deep neural network models for processing the TPP and FPP plots, because it helps preventing overfitting. Note that a ResNet-like (Residual Neural Network) CNN architecture works well in general image classification problems. We will show in Section 3 by evaluation that our VGG-PR and CNN-PR models slightly outperform the ResNet model and justify our choice. Both the kernels of the VGG-PR and CNN-PR models in our framework are large. Our practice shows that DCNNs with large convolution kernels work better in pulsar

candidate recognition, even though it has been claimed in the previous work (Simonyan & Zisserman 2015) that multiple small convolution kernels can achieve the same performance as a large convolution kernel.

Recurrent neural networks (RNN) are widely used in speech recognition and machine translation due to their ability of using the internal state (memory) to process sequences of inputs. Thus an RNN model, the long short-term memory (LSTM) proposed in Lakhil et al. (2018), is used to process the SPP sequence. The LSTM model has three control units, i.e., the input gate, the output gate, and the forget gate, which help the selective deletion and retention of information and make the LSTM model good at processing long dependency sequences. We also add a simple attention mechanism to LSTM, and thus the model is called the LSTM-A model (Long et al. 2018). As shown in Figure 7, the LSTM-A model consists of the bidirectional LSTM and the simple attention mechanism. Let the sequence of SPP be represented by an  $n \times 1$  vector. The bidirectional LSTM consists of  $n$  steps, and at each Step- $i$ , the  $i$ th element of the SPP vector is fed into the LSTM, where  $i = 0, 1, \dots, n$ . Let  $\xi_i$  denote the output vector of each Step- $i$ . The set of vectors  $\xi$  will be blended by the simple attention mechanism to form a single vector  $h_s$ . More specifically, the vector  $\beta$  is the learned weights through the attention mechanism.

$$\kappa_i = \frac{e^{\beta^T \xi_i}}{\sum_{j=0}^n e^{\beta^T \xi_j}}, i = 0, \dots, n. \quad (2)$$

Let  $\kappa_i$  denote the weight associated with the output vector  $\xi_i$ , and  $\kappa_i$  can be calculated as in Equation (2).

$$h_s = \sum_{i=0}^n \kappa_i \xi_i. \quad (3)$$

Finally, the integrated vector by the attention mechanism,  $h_s$ , i.e., the feature vector of the SPP sequence is calculated

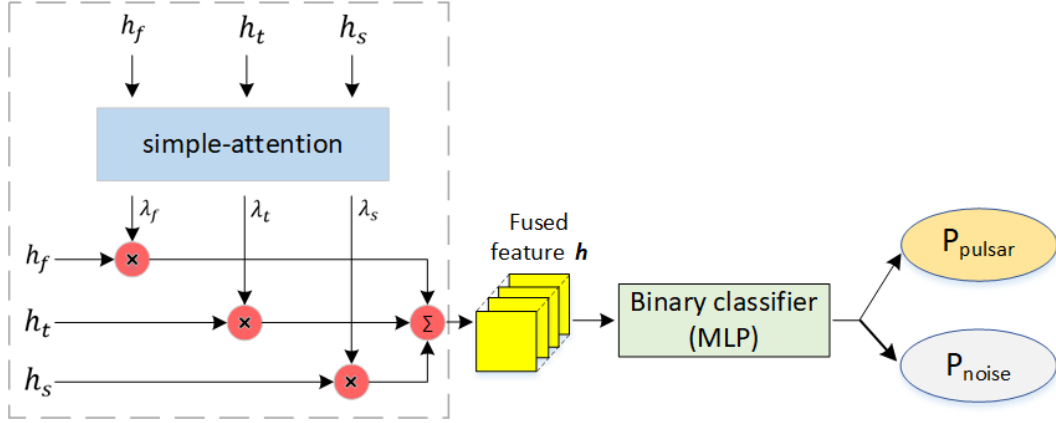


**Fig. 8** Stage 3 consists of a simple attention mechanism and a binary classifier. The feature vectors  $h_t$ ,  $h_f$  and  $h_s$  obtained at Stage 2 are fed into the simple-attention layer to produce a weight vector  $\omega$ . The weight vector  $\omega$  is used to blend the three feature vectors  $h_t$ ,  $h_f$  and  $h_s$  to form the attention vector  $h$ . The attention vector  $h$  is fed into the binary classifier (MLP) to produce the final sample category. The output is the probability that a sample is positive.

as in Equation (3). The feature vector  $h_s$  will enter Stage 3 with the other two features  $h_t$  and  $h_p$  of TPP and FPP, respectively.

### 2.2.1 Improved loss function for the imbalanced dataset and hard samples

Though a majority of noise data has been dropped at Stage 1, Stage 2 still faces the problem of imbalance.

$$L = y \log \hat{y} + (1 - y) \log(1 - \hat{y}). \quad (4)$$

A conventional cross entropy loss function defined in Equation (4) often leads to overfitting when the dataset is imbalanced. In Equation (4),  $\hat{y}$  is the probability that the label is positively predicted, and  $y$  is the ground truth label.

$$L = \alpha y \log \hat{y} + (1 - \alpha)(1 - y) \log(1 - \hat{y}). \quad (5)$$

In Equation (5), we introduce a weighting factor  $\alpha \in [0, 1]$  to address the class imbalance. The weight  $\alpha$  is often set as the inverse class frequency or a hyper-parameter by the cross validation in practice (Lin et al. 2020).

Except for the class imbalance problem, there exist hard samples as shown in Figure 3.

$$L = \alpha y(1 - \hat{y})^\gamma \log \hat{y} + (1 - \alpha)(1 - y)\hat{y}^\gamma \log(1 - \hat{y}). \quad (6)$$

Therefore we propose to reshape the loss function to down-weight easy examples and thus focus on training hard negatives as in Equation (6) (Lin et al. 2020). In Equation (6), the parameter  $\gamma$  controls the weight of difficult-to-classify samples in the training process.

### 2.3 Stage 3: Binary Pulsar Classification on Fused Features

At Stage 2, three feature vectors are obtained from the three diagnostic plots and need to be integrated before

entering the binary classifier. We propose to fuse features based on a simple attention mechanism proposed in Long et al. (2018). As shown in Figure 8, the feature vectors  $h_t$ ,  $h_f$  and  $h_s$  are fed into the simple-attention layer to produce a learned weight vector  $\omega$ . The weight vector  $\omega$  is the learned parameters in the attention mechanism. The attention mechanism in Stage 3 is mainly used to learn the weights of the three multidimensional features, and use the learned weights to blend the three features obtained from Stage 2 to form a single feature.

$$\begin{aligned} \lambda_t &= \frac{e^{\omega^T h_t}}{e^{\omega^T h_t} + e^{\omega^T h_f} + e^{\omega^T h_s}}, \\ \lambda_f &= \frac{e^{\omega^T h_f}}{e^{\omega^T h_t} + e^{\omega^T h_f} + e^{\omega^T h_s}}, \\ \lambda_s &= \frac{e^{\omega^T h_s}}{e^{\omega^T h_t} + e^{\omega^T h_f} + e^{\omega^T h_s}}. \end{aligned} \quad (7)$$

The weight vector  $\omega$  learned from the attention mechanism is further used to calculate the weights  $\lambda_t$ ,  $\lambda_f$ ,  $\lambda_s$  associated with the feature vectors  $h_t$ ,  $h_f$  and  $h_s$  as in Equation (7), respectively.

$$h = \lambda_t h_t + \lambda_f h_f + \lambda_s h_s. \quad (8)$$

After obtaining the weights  $\lambda_t$ ,  $\lambda_f$ ,  $\lambda_s$ , the integrated attention feature vector,  $h$ , can be calculated as in Equation (8). Finally, the attention vector  $h$  will be fed into a binary classifier, i.e., the multi-layer perceptron (MLP) to get the final sample category.

## 3 EXPERIMENTAL RESULTS

In this section, we present a comprehensive experiment on the HTRU-medlat dataset, and make a comparative analysis with the state-of-the-art results. The experiment is conducted on a GeForce GTX 1080 graphics card with the deep learning framework PyTorch (Ketkar 2017).

**Table 1** Percentage of Remaining Positive Samples with Different  $c$ 

$c$	recall of positive	recall of negative	filtering rate
200	48.2%	1.4%	2.05%
100	72.2%	2.7%	3.65%
50	97.8%	6.5%	7.82%
<b>43</b>	<b>99.8%</b>	<b>13.8%</b>	<b>15.00%</b>

### 3.1 Details of Experiment Setup

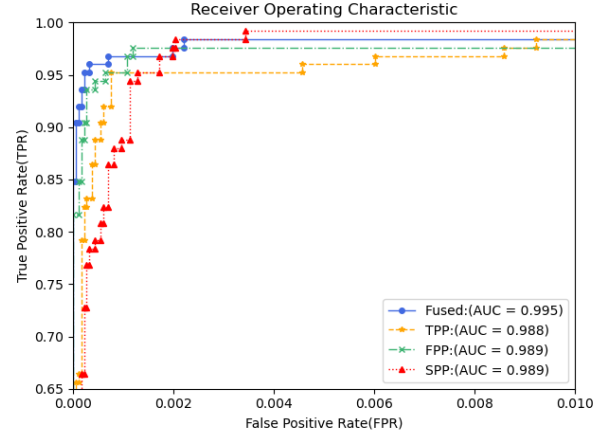
The HTRU-medlat dataset is first processed by the self-provided codes to generate TPP, FPP and SPP diagnostic plots. Secondly, the TPP or FPP plot is resized to a  $64 \times 64$  or  $48 \times 48$  matrix to fit the VGG-PR or CNN-PR model, respectively. The SPP plot is represented by a  $64 \times 1$  vector. Finally, all the elements of the TPP/FPP/SPP matrices or vectors are normalized to remove the absolute scale of the plots.

$$v_i = \frac{v_i - \mu}{\sigma}. \quad (9)$$

More specifically, for a vector  $v$ , each element  $v_i$  is recalculated as in Equation (9), where  $\mu$  and  $\sigma$  are the mean and standard deviation of the elements in vector  $v$ . For a matrix, normalization is performed by row vectors, which removes instrumental variations but remains the variance in signal (Zhu et al. 2014).

At Stage 1 of data cleaning, we need to tune the threshold  $c$  to keep more than 99% of positive candidates. As we discussed before, we do the smart under-sampling only using the FPP diagnostic plots. We flatten a  $48 \times 48$  FPP matrix to a  $2304 \times 1$  vector. The vector is further reduced to a  $32 \times 1$  vector by the technique of the principal component analysis (PCA) (Abdi & Williams 2010). All the samples are sorted in descending order according to the Mahalanobis distances, and the threshold  $c$  can be determined by keeping more than 99% of positive samples in the dataset.

In Table 1, we show the percentage of positive samples that remain in the dataset with different  $c$ . We choose  $c = 43$  and remain about 99.8% positive samples and 13.8% negative samples after cleaning. The filtering rate is defined as the number of remaining samples over the number of original samples. At Stage 2, the VGG-PR, CNN-PR and LSTM models follow three fully connected layers with hidden size 1024, 256, and 256, respectively. The activation function in fully connected layers is PReLU (He et al. 2015b). The obtained features are represented by three  $1024 \times 1$  vectors, respectively. At Stage 3, the model MLP consists of three fully connected layers with hidden size 1024, 256, and 256, respectively.

**Fig. 9** The ROC curves of classification based on the fused features or each individual feature.

### 3.2 Evaluation Criteria

$$\text{Recall} = \frac{\text{TP}}{\text{TP} + \text{FN}}, \quad (10)$$

$$\text{Precision} = \frac{\text{TP}}{\text{TP} + \text{FP}}, \quad (11)$$

$$F1 = 2 \times \frac{\text{Recall} \times \text{Precision}}{\text{Recall} + \text{Precision}}. \quad (12)$$

We use  $F1$  score to evaluate our approach considering the imbalance between positive samples and negative samples in HTRU medlat dataset (Yao et al. 2016). The  $F1$  score is defined as in Equations (10)–(12), where TP is the number of positive samples that are predicted as positive samples; FN is the number of positive samples that are predicted as negative samples; FP is the number of negative samples that are predicted as positive samples. We only evaluate the  $F1$  score for positive samples, because only efficient recognition of positive samples is meaningful in pulsar searching.

$$\text{TPR} = \frac{\text{TP}}{\text{TP} + \text{FN}}. \quad (13)$$

$$\text{FPR} = \frac{\text{FP}}{\text{TN} + \text{FP}}. \quad (14)$$

We also define the True Positive Rate (TPR) and False Positive Rate (FPR) as in Equation (13) and Equation (14), respectively. The TPR and FPR are used to plot the Receiver Operating Characteristic (ROC) curve, which can effectively evaluate the trained models of the unbalanced dataset (Carter et al. 2016). The area under the ROC curve (AUC) is a commonly used measure of the model's capability of distinguishing between classes. A higher AUC generally stands a better model at distinguishing between classes.



**Table 2** Experimental Results Compared with the State-of-the-art Works

	<i>F1</i> -score	Recall	Precision	time (min)
Guo et al. (2017)	0.96	0.96	0.96	$\approx 10^3$
Our approach	0.95	0.94	0.96	$\approx 10^2$
Zhang et al. (2019) (average results)	0.92	0.94	0.91	$\approx 10^2$
Our approach (average results)	0.95	0.95	0.96	$\approx 10^2$

**Table 3** Compare with the ResNet34 model

	VGG-PR/CNN-PR			ResNet34		
	<i>F1</i> score	Recall	Precision	<i>F1</i> score	Recall	Precision
TPP	0.95	0.96	0.94	0.94	0.94	0.93
FPP	0.92	0.93	0.90	0.91	0.91	0.91

**Table 4** Classification Based on the Fused Features vs Classification Based on Each Individual Feature

Feature	<i>F1</i> score	Recall	Precision
FPP	0.92	0.94	0.90
TPP	0.95	0.94	0.96
SPP	0.89	0.94	0.85
Fused Features	<b>0.96</b>	<b>0.95</b>	<b>0.97</b>

**Table 5** Comparison of Different Fusion Strategies

	<i>F1</i> score	Recall	Precision
concatenation	0.95	0.96	0.94
weighted summation	0.95	0.96	0.94
attention-based	0.96	0.97	0.95

**Table 6** The Improved Loss Function vs the Original Focal Loss Function

	<i>F1</i> score	Recall	Precision
Improved Loss Function	0.95	0.94	0.96
Original Loss Function	0.95	0.93	0.97

### 3.3 Detailed Results

In Table 2, we compare our approach with the state-of-the-art works in Guo et al. (2017) and Zhang et al. (2019). When we compare with the work in Guo et al. (2017), the HTRU medlat dataset after under-sampling is split into three parts with a ratio of 4 : 3 : 3, for training, validation and testing, respectively, and the results of a single test are reported. When we compare with the work in Zhang et al. (2019), we follow a 10-foldcross validation that is used in Zhang et al. (2019). In the 10-foldcross validation, the HTRU-medlat dataset after under-sampling is randomly split into 10 subsets, and nine subsets are used as the train sets and the 10th subset is used as the test set. The procedure is repeated randomly for 10 times and the average performance is reported in Table 2. As shown in

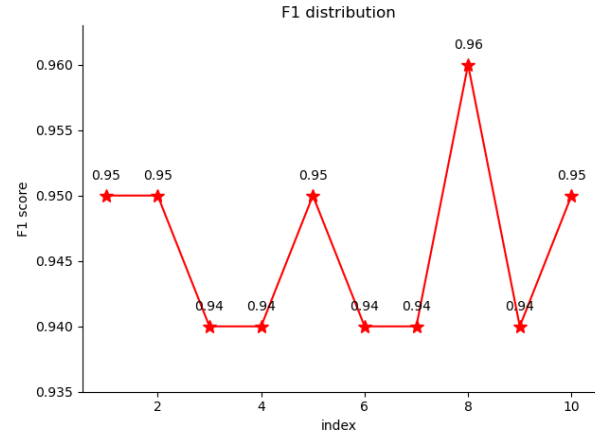
**Fig. 10** The performance results of 10 random experiments.

Table 2, the performance of our approach is comparable with that of Guo et al. (2017) in terms of *F1* score, Recall and Precision, and our approach improves the training time by  $10\times$ . Compared with the work in Zhang et al. (2019), our approach has a similar training time and outperforms it in all other criteria.

We justify the choice of VGG-PR model and CNN-PR model for processing the TPP and FPP plots, respectively. In the experiments, we replace the VGG-PR or the CNN-PR model by a ResNet34 model proposed in He et al. (2015a). Table 3 shows the performance of the ResNet34 model, which is not good enough compared with that of VGG-PR/CNN-PR.

Next, we evaluate the attention-based feature fusion strategy. We perform the classification based on each individual feature of TPP, FPP or SPP instead of the fused features obtained at Stage 3. we also follow the 10-fold cross validation. In Table 4, we compare the performance of classification based on the fused features with the classification based on each individual feature. It is obvious that the feature fusion based approach improves

all evaluation criteria including Recall, Precision and  $F1$  score greatly. In Figure 9, we present the ROC curves of the classification. Note that the TPR and FPR are calculated based on the original HTRU-medlat dataset. It shows that the classification with the fused features obtains a high TPR while maintains a low FPR and achieves the highest AUC. We further compare the attention-based feature fusion strategy with the concatenation and weighted summation fusion strategies proposed in Zhang et al. (2020). The concatenation strategy simply concatenates all the three features, and the weighted summation fusion strategy uses the weighted sum of the three features. We simply replace our attention-based feature fusion by the two candidate strategies in the experiments. Table 5 shows that the attention-based strategy achieves the best performance compared with the other two strategies. Overall, the proposed feature fusion benefits the pulsar candidate recognition.

We compare the performance of the improved loss function with the original focal loss function in Table 6. The results show that both the loss functions obtain the same  $F1$  score of 0.95. Nevertheless, the improved loss function can achieve a more balanced combination of Recall and Precision.

Finally, we evaluate the robustness of our approach by randomly splitting the dataset for 10 times. We report  $F1$  score of each individual test and the average performance of the tests in Figure 10. It shows that the average obtained  $F1$  score is about 95%, and all random tests achieve the  $F1$  scores around 94% – 96%.

#### 4 CONCLUSION

We propose a deep learning framework consisting of the smart under-sampling, early feature fusion and the improved loss function for pulsar recognition to cope with the class imbalance problem. Considering the  $F1$  score of positive samples and the training time, our framework can get a competitive result and speed up the training time by  $10\times$  compared with the state-of-the-art works. We conclude our unique contribution. First, we propose a strategy for under-sampling based on the Mahalanobis distance, which drops most of the negative samples. Secondly, we use the simple attention mechanism to fuse features extracted by the artificial neural networks. Thirdly, we improve the cross entropy loss function for the imbalanced class and hard negative sample issues. To our best knowledge, it is the first time that the improved loss function is used in pulsar recognition. All the techniques we proposed are not only helpful in pulsar identification, but also can be used to solve other extremely unbalanced problems.

**Acknowledgements** This work was supported in part by Science and Technology Commission of Shanghai Municipality, China (Grant No. 19ZR1463900) and the National Key R&D Programme of China (Grant No. 2018YFA0404603).

#### References

- Abdi, H., & Williams, L. J. 2010, WIREs Computational Statistics, 2, 433
- An, T. 2019, Science China Physics, Mechanics, and Astronomy, 62, 989531
- Carter, J. V., Pan, J., Rai, S. N., & Galandiuk, S. 2016, Surgery, 159, 1638
- Chaib, S., Liu, H., Gu, Y., & Yao, H. 2017, IEEE Transactions on Geoscience and Remote Sensing, 55, 4775
- Chawla, N. V., Bowyer, K. W., Hall, L. O., & Kegelmeyer, W. P. 2002, J. Artif. Int. Res., 16, 321
- Cordes, J. M., Freire, P. C. C., Lorimer, D. R., et al. 2006, ApJ, 637, 446
- Gao, J., Gong, L., Wang, J. Y., & Mo, Z. C. 2018, in 2018 IEEE International Conference on Industrial Engineering and Engineering Management (IEEM), 1538
- Gunes, H., & Piccardi, M. 2005, in 2005 IEEE International Conference on Systems, Man and Cybernetics, Vol. 4, 3437
- Guo, P., Duan, F., Wang, P., et al. 2017, arXiv e-prints, arXiv:1711.10339
- Han, H., Wang, W.-Y., & Mao, B.-H. 2005, in Proceedings of the 2005 International Conference on Advances in Intelligent Computing – Volume Part I, ICIC’05 (Berlin, Heidelberg: Springer-Verlag), 878
- He, H., Bai, Y., Garcia, E. A., & Li, S. 2008, in 2008 IEEE International Joint Conference on Neural Networks (IEEE World Congress on Computational Intelligence), 1322
- He, K., Zhang, X., Ren, S., & Sun, J. 2015a, arXiv e-prints, arXiv:1512.03385
- He, K., Zhang, X., Ren, S., & Sun, J. 2015b, in 2015 IEEE International Conference on Computer Vision (ICCV), 1026
- Hubert, M., & Debruyne, M. 2010, Wiley Interdisciplinary Reviews Computational Statistics, 2, 36
- Keane, E. F., Ludovici, D. A., Eatough, R. P., et al. 2010, MNRAS, 401, 1057
- Keith, M. J., Jameson, A., van Straten, W., et al. 2010, MNRAS, 409, 619
- Ketkar, N. 2017, Introduction to PyTorch, Deep Learning with Python: A Hands-on Introduction (Berkeley, CA: Apress), 195
- Lakhal, M. I., ?evikalp, H., Escalera, S., & Ofli, F. 2018, IET Computer Vision, 12, 1040
- Li, S., Feng, S., Guo, P., & Yin, Q. 2018, in 2018 IEEE Congress on Evolutionary Computation (CEC), 1
- Lin, T., Goyal, P., Girshick, R., He, K., & Dollár, P. 2020, IEEE Transactions on Pattern Analysis and Machine Intelligence, 42, 318

- Liu, X., Wu, J., & Zhou, Z. 2009, *IEEE Transactions on Systems, Man, and Cybernetics, Part B (Cybernetics)*, 39, 539
- Long, X., Gan, C., de Melo, G., et al. 2018, in *Proceedings of the Thirty-Second AAAI Conference on Artificial Intelligence (AAAI-18), the 30th innovative Applications of Artificial Intelligence (IAAI-18), and the 8th AAAI Symposium on Educational Advances in Artificial Intelligence (EAAI-18)*, New Orleans, Louisiana, USA, February 2-7, 2018, eds. S. A. McIlraith & K. Q. Weinberger (AAAI Press), 7202
- Morello, V., Barr, E. D., Bailes, M., et al. 2014, *MNRAS*, 443, 1651
- Padma, S., Kumar, S. S., & Manavalan, R. 2011, in *2011 6th International Conference on Industrial and Information Systems*, 300
- Simonyan, K., & Zisserman, A. 2015, *International Conference on Learning Representations*
- Tomek, I. 1976, *IEEE Transactions on Systems, Man, and Cybernetics*, SMC-6, 448
- Vannucci, M., & Colla, V. 2016, in *Intelligent Decision Technologies 2016*, eds. I. Czarnowski, A. M. Caballero, R. J. Howlett, & L. C. Jain (Springer International Publishing), 395
- Vannucci, M., & Colla, V. 2017, in *Intelligent Decision Technologies 2017*, eds. I. Czarnowski, R. J. Howlett, & L. C. Jain (Springer International Publishing), 23
- Vannucci, M., & Colla, V. 2018, in *2018 International Joint Conference on Neural Networks (IJCNN)*, 1
- Wang, D., Yin, Q., & Wang, H. 2017a, in *Intelligence Science I*, eds. Z. Shi, B. Goertzel, & J. Feng (Cham: Springer International Publishing), 241
- Wang, F., Jiang, M., Qian, C., et al. 2017b, in *2017 IEEE Conference on Computer Vision and Pattern Recognition (CVPR)*, 6450
- Wang, H., Zhu, W., Guo, P., et al. 2019, *Science China Physics, Mechanics, and Astronomy*, 62, 959507
- Wilson, D. L. 1972, *IEEE Transactions on Systems, Man, and Cybernetics*, SMC-2, 408
- Yao, Y., Xin, X., & Guo, P. 2016, in *2016 12th International Conference on Computational Intelligence and Security (CIS)*, 120
- Zhang, X., Shi, Z., Liu, X., & Li, X. 2018, in *2018 IEEE International Conference on Smart Internet of Things (SmartIoT)*, 269
- Zhang, H., Zhao, Z., An, T., Lao, B., & Chen, X. 2019, *Computers and Electrical Engineering*, 73, 1
- Zhang, C., Yang, Z., He, X., & Deng, L. 2020, *IEEE Journal of Selected Topics in Signal Processing*, 14, 478
- Zhou, B., Wang, T., Luo, M., & Pan, S. 2017, in *2017 Eighth International Conference on Intelligent Control and Information Processing (ICICIP)*, 49
- Zhu, W. W., Berndsen, A., Madsen, E. C., et al. 2014, *ApJ*, 781, 117